Available online at www.sciencedirect.com
SCIENCE DIRECT
Planetary and Space Science 54 (2006) 645–660
Planetary and Space Science
www.elsevier.com/locate/pss

A laser altimeter for BepiColombo mission: Instrument design and performance model

Maria Rosaria Santovito[a,*], Leonardo Tommasi[b], Germano Sgarzi[c], Andrea Romoli[b], Stefania Mattei[a], Eamonn Murphy[d], Nicola Rando[d]

[a]Co.Ri.S.T.A. Consortium for Research on Advanced Remote Sensing Systems, viale J.F. Kennedy 5, I-80125 Naples, Italy
[b]Galileo Avionica, via A. Einstein 35, I-50013 Campi Bisenzio (Florence), Italy
[c]Galileo Avionica, via dei Castelli Romani 2, I-00040 Pomezia (Rome), Italy
[d]European Space Agency, ESTEC, Keplerlaan 1, NL-2201 Noordwijk, The Netherlands

Received 20 May 2005; received in revised form 13 March 2006; accepted 22 March 2006
Available online 9 May 2006

Abstract

This paper presents a definition study of a laser altimeter for the topographic exploration of Mercury. The reference scenario is the BepiColombo mission, a cornerstone mission of European Space Agency (ESA) planned for 2012. BepiColombo will offer the chance to make a remarkable new contribution to our knowledge of the Solar System, by venturing into the hot region near the Sun and exploring Mercury, the most enigmatic of the earth's sisters among the terrestrial planets. First images of Mercury surface were acquired by Mariner 10 in 1974 and 1975 offering a coverage and resolution comparable to Earth-based telescopic coverage of the Moon before spaceflight. BepiColombo mission can be very beneficial by using an optical rangefinder for Mercury exploration. In fact starting from the first missions in 1970s until today, laser altimeters have been demonstrating to be particularly appropriate as part of the scientific payload whenever the topography of earth, lunar and planetary surface is the scientific objective of a space mission.

Our system design is compliant to Mercury Polar Orbiter (MPO) of the mission. System performance analysis is carried out simulating main hermean topographic features and the potential targets on the planet by means of analytical models and computer codes and several plot are presented to analyse the performance of the instrument.

Keywords: Mercury; Topography; Laser altimeter; BepiColombo mission

1. Introduction

Recently a laser rangefinder has been considered for an European Space Agency (ESA in the following) cornerstone mission: the BepiColombo mission to Mercury (Murphy et al., 2003).

The main scientific objectives of BepiColombo mission are (ESA, 2000):

- morphology, geology, cratering and surface composition of Mercury;
- planetary magnetic field, rotational state and interior structure of Mercury and
- general relativity and gravitation.

The mission will send to the planet two orbiters:

- Mercury Polar Orbiter (MPO) dedicated to planet wide remote sensing, radio science and asteroids observations and
- Mercury Magnetospheric Orbiter (MMO) accommodating mostly the field, wave and particle instruments.

BepiColombo will be the first mission with dual Mercury orbiters and the first European deep-space probe using electric propulsion.

*Corresponding author. Tel.: +39 081 5939073x231; fax: +39 081 5933576.
E-mail address: santovit@unina.it (M.R. Santovito).

0032-0633/$ - see front matter © 2006 Elsevier Ltd. All rights reserved.
doi:10.1016/j.pss.2006.03.003

The MPO and the MMO composites will be launched in 2012 and will reach Mercury in 3.5 years. First images of Mercury surface were acquired by Mariner 10 in 1974 and 1975 (Neukum et al., 2001; Watters et al., 2001; Robinson and Lucey, 1997). The best resolution of 2500 images was around 100 m but less than 1% of the surface was covered at a resolution of better than 500 m and less than 50% coverage was obtained at a resolution between 1 and 1.5 km. This coverage and resolution is modest and comparable to Earth-based telescopic coverage of the Moon before spaceflight.

BepiColombo mission can be very beneficial by using an optical rangefinder for Mercury exploration. The technique can provide accurate information on the surface profile in a fast and cost effective manner in comparison with RF system (Mattei et al., 2006), and allowing, within the characteristics of spacecraft orbit, global coverage of the planet surface.

The basis of the laser altimeter measurement is the timing of short pulses for round-trip propagation at the speed-of-light between the space probe and the surface to be measured (Bufton, 1989; Forrester and Hulme, 1981). Laser altimetry can provide measurements of the structure and albedo of the target surface in addition to the straightforward range measurement (Gardner, 1992; Abshire et al., 2000). Surface structure (i.e. the height distribution or slope within the laser footprint) is determined by the analysis of the backscattered laser pulse shape through analogue processing or high-speed digitisation. The transmitted laser pulse width is typically optimised to be very short (1–10 ns) for high-precision ranging. After interaction of the laser footprint with a rough or sloping surface, the backscattered pulse may contain several nanoseconds or more of pulse spreading or distortion. The application of gigahertz bandwidth digitisation to this received pulse waveform provides pulse shape data. The backscattered pulse width (or rms pulse spreading) that is derived from these data is usually a sufficient measure of surface structure. The total area under the received pulse is proportional to the pulse energy and it is a measure of surface albedo at the monochromatic laser wavelength. Effective use of this albedo data requires at least a calibration of laser backscatter from different surfaces and a normalisation by laser transmitter energy.

From 1971 to 72, when three Apollo missions carried laser altimeters to the Moon, to the Mars Global Surveyor mission operating the MOLA (Mars Orbiter Laser Altimeter) instrument for nearly 1000 days, the number of planetary ranges has increased by more than five orders of magnitude, and accuracy by nearly three orders. High-resolution Moon contour maps were created from Apollo orbiters metric camera stereo images, using control from laser altimeters (Margot et al., 1999). Coverage was modest, laser transmitters were short-lived but the Apollo altimeters were adequate for their primary purpose, giving ranges for photographs, with a precision of about 4 m. Two decades after the Apollo orbiters, a Laser Image Detection and Ranging (LIDAR) experiment was designed to measure the distance from the spacecraft to a point on the surface of the Moon (Nozette et al., 1994; Smith et al., 1997) and flown on Clementine, a joint mission of NASA (National Aeronautics and Space Administration) and the Ballistic Missile Defence Organisation. This allowed an altimetric map to be made, which can be used to identify the morphology of large basins and other lunar features. SLA-01 was the first of four planned flights to precisely measure the distance to the Earth's surface from the Space Shuttle. SLA-02 emitted laser pulses and measured their echoes from the Earth to determine the shape of land surfaces and vegetation canopies. SLA-01 and SLA-02 demonstrated the effectiveness of orbital laser altimeters for terrestrial geodesy despite relatively short flights and the inconvenience of using the shuttle as an orbital platform (Garvin et al., 1998). In February 2000 the NEAR (Near-Earth Asteroid Rendezvous) spacecraft, which carried the NEAR Laser Range (NLR), reached the asteroid 433 Eros, one of the largest and most intensively studied near-Earth asteroids (Cheng et al., 2000; Cole, 1998). The overall NEAR mission objective was to provide information about the origin and nature of near-Earth asteroids, whose characteristics are suspected to provide clues about the formation of the inner planets, including the Earth. The NLR made highly accurate measurements of asteroid's shape and detailed surface capability. In September 1997, the Mars Global Surveyor (MGS) entered into orbit around Mars. One of the four scientific instruments on MGS was the Mars Orbiter Laser Altimeter (MOLA) which mapped the topography of the planet to unprecedented accuracy (Abshire et al., 2000; Neumann et al., 2001). The primary objective of the MOLA investigation was to determine the global topography of Mars for addressing fundamental questions in planetary geology and geophysics. Secondary objectives was the study of the 1064 nm surface reflectivity of Mars, to contribute to analyses of global surface mineralogy and seasonal albedo changes, to assist in addressing problems in atmospheric circulation, and to provide geodetic control of topography for assessing future Mars landing sites. In August 2004, NASA's Discovery programme launched MESSENGER (MErcury Surface, Space, ENvironment, GEochemistry and Ranging) spacecraft with Mercury Laser Altimeter (MLA) and other six scientific instruments on board. The goal of MESSENGER mission is to analyse the planet Mercury in order to understand how terrestrial planets formed and evolved (Solomon et al., 2001). MLA will start its observations on 2011 measuring the topography of the Mercury northern hemisphere via laser pulse time-of-flight (TOF). The primary science objectives are to provide a high-precision topographic map of the polar region, measure the long-wavelength topographic features of the mid-to-low latitude region, and to detect and to quantify the planet's forced librations (Sun et al., 2004). The laser design is on the heritage of MOLA technology but incorporates peculiar thermal management features

Table 1
Main features of already flown laser altimeters (Clementine, NLR and MOLA) and of MLA, which will start its observations around Mercury on 2011

	Clementine	NLR	MOLA	MLA
Pulse energy (mJ)	171	15.6	42	20
Pulse width FWHM (ns)	10	15	8	6
Laser beam divergence (μrad)	500	235	370	80
Pulse repetition frequency (Hz)	1	1/8, 1, 2,8	10	8
Receiver telescope diameter (cm)	13.1	7.62	50	11.5 × 4
Receiver telescope FOV	4 μrad	3 μrad	0.85 μrad	0.4 mrad
Orbit height (km)	500	160	400	400
Range resolution	40 m	32 cm	30 cm	15 cm
Instrument mass (kg)	2.37	4.9	26.2	7.4
Instrument power consumption (W)	6.8	15.1	28	23

due to the requirements of an orbit of the planet Mercury (Krebs et al., 2005).

MLA, MOLA and NLR, along with the laser altimeter of the lunar mission Clementine, represent a new class of active remote sensing instruments for conducting science in the solar system. A summary of the main features of these instruments are reported in Table 1.

All of them make use of a Nd:YAG laser operating at the wavelength of 1064 nm to generate pulses to be reflected by the planetary surface and adopt a silicon Avalanche Photodiode (Si APD) as a detector. Pulse repetition frequencies are different, according to the scientific and technical requirements of the missions.

In this work, after a review of the main hermean topographic features and the potential targets of laser altimetry on the planet, a preliminary design of the system with a low technological risk approach and a detail level compatible with a feasibility study, is presented. Then performance of the instrument (named LAPE: Laser Altimeter for Planetary Exploration) are analysed by taking into consideration the reference scenario of Bepi-Colombo mission.

2. Main hermean features and geological area of interest

Mariner 10 images indicate that Mercury and the Moon share striking similarities in the main geological features (Neukum et al., 2001). The cratering pattern, for example, is essentially the same, with presence of young and old features, sometimes associated to ring-like structures. Large, smooth and uncratered plains appear on both surfaces. The Moon can therefore represent a good model for the expected geological characteristics of Mercury. The main geologic features to be mapped by the BepiColombo laser altimeter are:

- highlands;
- lowland plains;
- impact basins;
- craters;
- lineaments and
- lobate scarps.

The first four are generally associated with impacts and, possibly, also volcanism. In this respect they do not differ substantially from the corresponding lunar features. The last two are traced to ancient tectonism. Today Mercury does not show signs of ongoing tectonic activity, but its remnant is clearly identified in Mariner 10 images.

Potential targets of laser altimeter could be lowlands plains, impact basins and lobate scarps.

The lowlands plains are young features with small crater density. In many aspects they are similar to the lunar *maria*, without exhibiting the same albedo variation with respect to the surrounding terrain. The lowlands show ridges and smooth plains. The similarity to the lunar *maria* suggests a volcanic origin, but other formation mechanisms have been proposed. Laser altimeter measurements are a key to clarify lowlands origins.

It is estimated that at least 50 large impact basins, with size larger than 200 km, occur on the hermean surface. They are old and young structures. The larger (diameter > 400 km) are multi-ringed (i.e. show more than two rings). In general, the younger impact basins exhibit a rugged terrain, with many small scale, km-size structures. This area is currently interpreted as induced by seismic waves propagating across the planet. These waves may have induced an uplift of several tens of metres, which in turn has generated a number of local rearrangements of the hermean crust.

The frequently occurring lobate scarps are tectonic structures and probably one of the most striking features of the hermean surface. They are deep, long (up to several hundred kilometres) huge faults and scarps originated by the cooling of the planet's crust. The available topographic data indicate that Discovery Rupes has the greatest relief (around 1.5 km), followed by Adventure Rupes (around 1.3 km) and Resolution Rupes (around 0.9 km). Dip angles are estimated to be in the range of 25°–45°.

Values of hermean surface slope can be found in literature but at our best knowledge no data on Mercury roughness are available. The surface roughness is usually indicated as $\mathrm{Var}(\Delta\zeta)$ because the surface slope is determined by the best fit plane which approximate the terrain and the roughness is the variance of the slope mean value. To have a rough estimation of Mercury variance roughness

$\mathrm{Var}(\Delta\zeta)$ in our model we used the values of terrestrial roughness (Harding et al., 1994) of terrains with geomorphic characteristics similar to the expected characteristics of Mercury surface. In our performance analysis the roughness ranges from 1 to 6 m, values quantified by Harding et al. at a length scale of 186 m, compatible with LAPE footprint diameter for an altitude around 900 km.

3. Instrument design

Instrument design follows the drivers of the BepiColombo ESA mission, namely low mass and power demand, high modularity approach for possible integration in a payload suite and compatibility to the harsh Mercury environment, with proper shield of thermal input from the hot planetary surface (Murphy et al., 2003). However, the design is oriented to achieve high performance in terms of detection probability and ground resolution, as well as capacity to measure range to surface, albedo, and ground slope. Finally, a low-technological risk solution, compatible with a short development and realisation time, is proposed, at a detail level compatible with a feasibility study. Even if some aspects require further investigation (e.g. thermal and electronics design), we believe that the present design is appropriate at a system level and can provide all the relevant inputs to the following performance model. The selected measurement approach is based on high signal-to-noise ratio (SNR)/single-pulse detection probability. Although techniques based on statistical analysis of received pulses exist to cope with a lower detection probability, a high detection probability to allow single-pulse detection has been chosen to achieve the highest possible along track spatial resolution. This requires false alarm rate to be kept low, to avoid wrong data interpretation due to unrealistic altitude values. However, since it is also demonstrated by our performance analysis, a low false alarm rate implies lower detection probability, so a trade off is proposed and evaluated herein.

3.1. Subsystems identification

A functional block diagram of the laser altimeter is illustrated in Fig. 1 where instrument subsystems are intended as separate physical units.

In fact, in an integrated instrument approach, such as that envisaged for the BepiColombo MPO spacecraft, the instrument front end, including only those functions that cannot be performed at a centralised level, could be best realised as a set of modules to be integrated within the spacecraft payload, as it is better explained in the following. In this approach, interfaces between the LAPE units and between them and the rest of the spacecraft appear as a critical issue, that needs further definition starting from the phase A of each payload instrument definition. On the other hand, this approach could allow to reduce mass, volume and power consumption.

The following five units have been identified as components of the LAPE design:

- Transmitter unit (TXU);
- Thermal shield unit (TSU);
- Receiver unit (RXU);
- LAPE electronics unit (LEU) and
- Power supply unit (PSU).

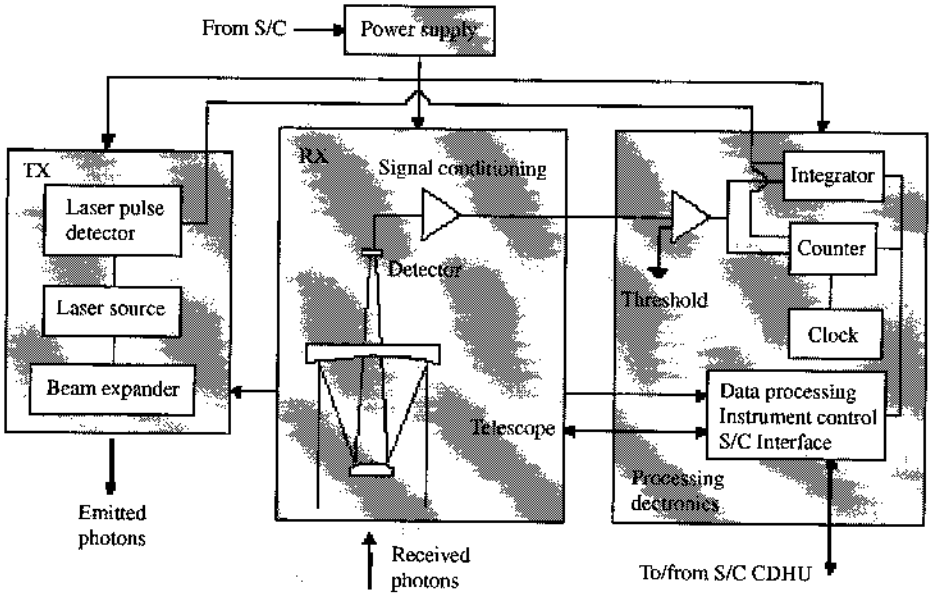

Fig. 1. LAPE functional block diagram. CDHU is for Command and Data-Handling Unit.

Table 2
LAPE TXU specifications

Laser pulse energy (mJ)	80
Laser pulse duration (ns)	10
Laser beam divergence (after BE) (μrad)	200
Laser beam angular stability (μrad r.m.s)	<10
Laser electrical-optical efficiency (%)	6
Laser wavelength (nm)	1064.4±0.1
Pulse repetition frequency (Hz)	16 (burst mode)
Size (mm^3)	300 × 160 × 110
Mass (kg)	2.2
Power (W)	15 in measurement mode <5 in stand-by mode

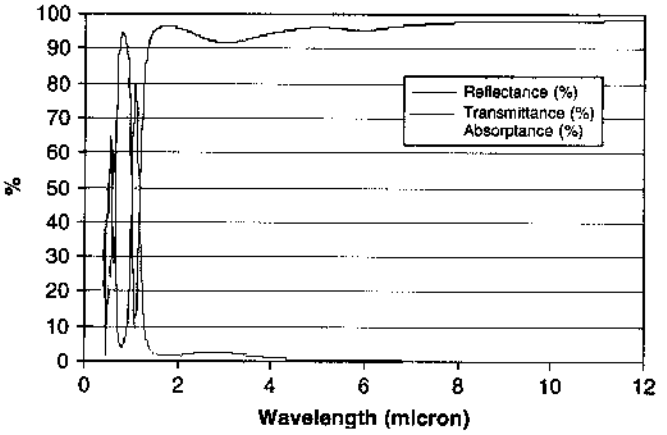

Fig. 2. Optical properties of the hybrid dielectric-gold coating.

Table 3
LAPE TSU specifications

Thermal shield architecture	4 × (Sun shield + coated window)
Shield material	Carbon fibre
Window material	Sapphire
Coating	Hybrid dielectric-gold
Heat rejection overall efficiency (%)	99.65
Cover operation	Single opening
Mass (kg)	2.4
Size (mm^3)	<300 × 300 × 200

3.1.1. Transmitter unit

TXU includes the laser transmitter, devoted to the generation of light pulses to be backscattered by the planetary surface under observation.

A Nd:YAG diode pumped laser source with electrically activated active Q-switch has been selected due to relative maturity of its technology for space applications. Other sources have been considered and traded off during the study as fibre lasers or micro-lasers, but have been discarded due to their immaturity being still at a laboratory bread board development level. The instrument-working wavelength is that of the laser at 1.064 μm. The transmitter is expected to work in a burst mode, alternating stand-by low power mode without laser emission and full performance mode at 16 Hz Pulse Repetition Frequency. Peak energy is established in 80 mJ and beam divergence is 200 μrad. The required beam divergence is met through the adoption of a Galilean beam expander, with a magnification of about 7.5. From a thermal point of view, a cold plate with temperature of 21±1 °C is assumed as interface with the spacecraft. Maximum heat power to be dissipated is 15 W. The specifications of TXU subsystem are summarised in Table 2.

3.1.2. Thermal shield unit

TSU is designed for the application of the LAPE in a thermally hostile environment, such as represented by a mission in orbit around Mercury due to its closeness to the Sun.

In particular, TSU has been investigated and dimensioned basing on the environmental requirements of the BepiColombo mission for the MPO. The concept is based on a twofold shielding approach (sun shield to reduce acceptance angle plus coated window to reject most part of the IR radiation), with an additional cover to protect the optics during the launch and cruise phase. The shield is realised in carbon fibre to minimise its mass, and should have a ratio between length and diameter equal or larger than 1.3 to allow rejection of direct sun light in the worst conditions (sun 38° from the line of sight). It has to be thermally insulated from the spacecraft wall (and so from the rest of payload) by means of a suitable mechanical interface (e.g. non-conductive washers). With this design the thermal load of the shield to the spacecraft can be considered negligible. Due to the 4 sub-telescopes approach selected for the RXU (see Section 3.1.3), even the TSU is composed by four identical sub-units. The protective cover is designed as a single-operation one (either to be opened or jettisoned) to minimise its complexity, criticality and mass. A lightweight material has to be adopted, carbon fibre is assumed as a baseline. The window is realised in sapphire, for the maximum thermal conductivity, and is covered with a multilayer hybrid gold-dielectric coating to reject (mainly by reflection) most of infra-red radiation above 2 μm still allowing high transmission at the laser wavelength. Coating features are summarised in Fig. 2, while specifications of the whole TSU are contained in Table 3.

TSU efficiency and the resulting thermal load from the hot planetary surface on the spacecraft are summarised in Fig. 3. Worst case is considered, namely: Mercury at perihelion, spacecraft at periherm, Sun at the zenith of the subsatellite point. Moreover, total radiation flux (emitted infra-red due to surface temperature plus reflected Sun irradiance) has been integrated over full visible planetary disc and whole UV to mid-infra-red spectral range.

3.1.3. Receiver unit

The RXU optical layout, as it is shown in Fig. 4, is made of a cluster of four focusing telescopes, a bundle of fibre optics, and a collecting optics.

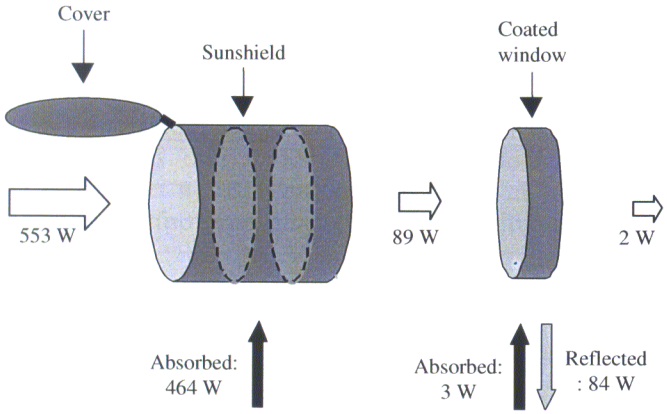

Fig. 3. Thermal load due to planetary radiation in the worst operative conditions (perihelion, maximum albedo, minimum altitude, local noon) and TSU efficiency.

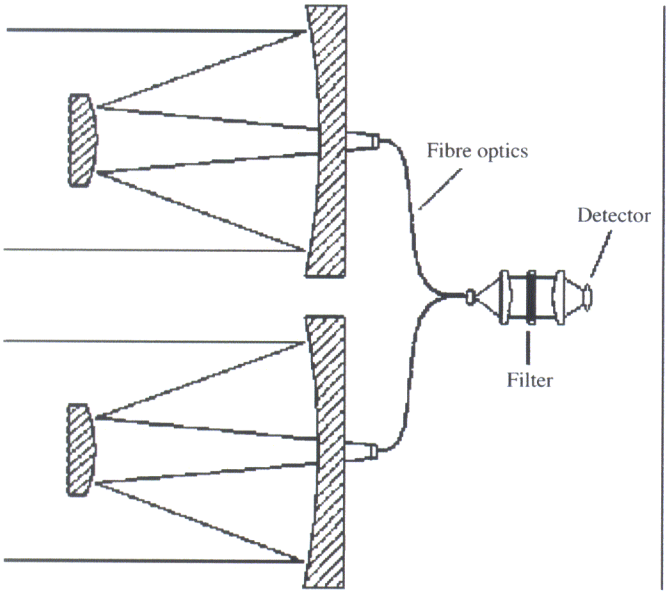

Fig. 4. Optical layout of the RXU (only two of the four telescopes are shown for simplicity).

The choice to split the required aperture into a number of sub-apertures allows to save a large amount of mass, since both the mass of optical elements and mechanical structures scales down roughly as the number of sub apertures. Each of the four co-aligned telescopes receives the backscattered power pulse onto a single fibre optics of a bundle. The other end of the bundle is collimated by a suitable lens, and the parallel beams coming from each fibre cross a narrow band interference filter matching the laser wavelength of 1.064 μm. Active temperature control of the filter is not envisaged within the operative temperature range of the BepiColombo payload. After the filter, the beams are focused onto a single detector.

The telescope has a Cassegrain design and could be suitably realised by using silicon carbide mirrors to achieve the lightest mass.

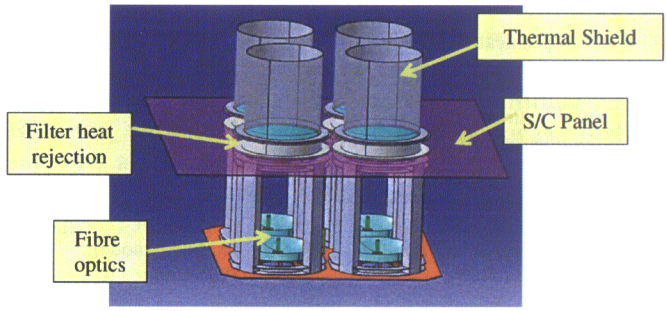

Fig. 5. View of TSU and RXU assembly.

Table 4
LAPE RXU specifications

Optics aperture (mm ∅)	4 × 125
Focal length (mm)	500
Optics material	SiC
Optical design	Cassegrain
Detector type	Silicon APD
Quantum efficiency (%)	40
Dark current amplifier noise (pA 1 pA/$Hz^{1/2}$)	10
Useful detector size (mm ∅)	1
Focal plane adapter (μm)	4 × 200 fibre optics assembly
Optics transmission	0.85
Filter transmission	0.625
Filter FWHM band (nm)	3
Mass (kg)	1.9
Size (mm^3)	$<300 \times 300 \times 250$
Power (W)	1

A Silicon APD detector is selected as a baseline to lower the risk associated to the instrument, following the selection made for all the past laser altimeters. This kind of detector exploits the high responsivity and fast response that are needed for ranging applications. In particular a module including also preamplifier and thermal compensation to allow the APD to work with constant gain within a large temperature range is envisaged.

A view of the TSU and RXU assembly is reported in Fig. 5.

The RXU specifications are summarised in Table 4.

3.1.4. *LAPE electronic unit*

LAPE electronics is subdivided into two functional and physical blocks:

- range measurement electronics (RME) and
- instrument control electronics (ICE).

The RME is devoted to received signal processing (analogue processing based on leading-trailing edge centroid estimation is selected since allocated resources are not compatible with e.g. pulse digitisation) up to the extraction of all the relevant physical information, namely:

- range (through TOF measurement),
- albedo (through ratio between transmitted and received energy),

Table 5
LAPE LEU specifications

Architecture	Most functions integrated in FPGA/ASIC
Functions	Measure range/slope/albedo
Oscillator frequency (MHz)	150
Oscillator stability (ppm)	<0.1
Mass (kg)	1.2
Size (mm^3)	170 × 235 × 150
Power (W)	10 (in measurement mode) <5 (in stand-by mode)
Data rate (bps)	752 (in measurement mode) only housekeeping (in stand-by mode)

- surface slope (through pulse width measurement).

The ICE is in charge of all the auxiliary instrument functions, that are:

- temperature control/regulation,
- instrument timing and clock generation,
- data packetisation,
- transition between operative modes management and
- spacecraft interface.

Even if some of the functions of the ICE can be quite easily integrated in the central payload electronics, a microprocessor will be needed within the front-end electronics to manage both high-speed processing and automatic mode transitions. LAPE range measurement electronics specifications are reported in Table 5.

Note that a coarse range acquisition mode is implemented, to be used for target acquisition in case of poor initial range knowledge. This is obtained by adopting a large range gate interval (T_{RG}), and performing statistical processing of a set of successive range acquisitions (histogram, 20 bins supposed herein) to reject the consequent large number of false alarms, resulting in a poor space resolution. Transitions from coarse acquisition to full performance science mode and viceversa are automatically managed by the LAPE electronics according to the results of the last performed range measurements.

3.1.5. Power supply unit

A LAPE power supply is devoted to the electric supply of the instrument subsystems, starting from a standard 28 V line from the spacecraft. The functions to be performed by the PSU are:

- low voltage for analogue and digital electronics supply,
- high-voltage line to drive laser diodes through capacitors,
- high voltage for APD bias,
- high voltage for active Q-switch operation and
- transitions between operative modes.

Actually, since a Central Payload Power Supply is foreseen in case of an integrated instrument approach as in the case of BepiColombo HIPS (High Integrated Payload Suite), we consider that the low voltage for analogue and digital electronics supply are in charge of this central unit, only regulation being demanded if necessary to the front-end PSU. On the other hand, all the high-voltage functions, that are peculiar of the laser altimeter, cannot be easily integrated and shall be performed by the LAPE PSU. The PSU specifications are reported in Table 6.

3.2. Budgets

Table 7 reports the LAPE mass budget.

Following the requirements for the MPO payloads the instrument mass has been reduced as much as possible by assuming a high degree of integration. In this approach no mechanical structure or bench is foreseen to integrate LAPE units in a self-standing payload instrument and the largest possible amount of power supply and instrument control functions is demanded to the corresponding centralised spacecraft units. Finally, no shield has been considered for the LAPE electronic units (LEU and PSU), in a scenario in which shielding from high-energy particles is realised at a common payload level. On the other hand, if the required shielding capacity was to be entirely realised at instrument front-end level, the worst case in terms of mass would be represented by an aluminium box hosting both the LEU and the PSU. The mass of this box would be about 1.6 kg. Different solutions shall be evaluated and traded off further on during the altimeter design to reduce this mass at a minimum level.

In Table 8 LAPE power budget is reported for each operative mode, taking into account the power

Table 6
LAPE PSU specifications

Input (V)	+28
Outputs (V)	±5 +10 +100 (LD capacitors) +500 (APD bias) +1000 (Q-switch)
Efficiency (%)	70
Mass (kg)	0.8
Size (mm^3)	200 × 270 × 60
Input voltage (V)	+28
Power (W)	<15 (in stand-by mode) 37 (in measurement mode)

Table 7
LAPE mass budget (figures include 20% contingency)

TXU (kg)	2.2
RXU (kg)	1.9
TSU (kg)	2.4
LEU (kg)	1.2
PSU (kg)	0.8
LAPE (kg)	8.5

Table 8
LAPE power budget and data rate

Mode	Description	Power range (W)	Data rate (bps)
Off	All units off.	0	0
Survival	Survival temperatures maintained	1–3	0
Temperature setting	Nominal temperatures reached	3–10	0
Stand-by	CPU is on RME is off TXU is off RXU is off	10–15	Housekeeping only
Init/ready	Transition mode	—	—
Measurement	CPU is on RME is on TXU is on RXU is on	37	752

consumption of the different sub-systems described above. Analogously to power, Table 8 reports also data rate budget for each operative mode.

It has to be observed that the power in measurement mode, while all LAPE units are on, exceeds the required MPO average value (30 W). However, the instrument is not expected to work at full performance over the whole orbit. Operation whenever the spacecraft altitude is lower than 1250 km (about 66% of each orbit around periherm) is sufficient to meet the requested average power budget.

Similar considerations can be done about data rate requirement compliance. In fact, full data rate in measurement mode exceeds the average data rate (500 bps). Aforementioned operation strategy along each orbit makes possible to match the required data rate with minor impact on the amount of collected data.

4. LAPE performance model

In our model we consider the following basic configuration for the LAPE:

- nadir pointing instrument,
- single-shot range measurement,
- the output of the APD is low-pass filtered to improve SNR and the ranging resolution (R_r) and then compared against a predetermined threshold level with the use of a discriminator. Following MOLA receiver subsystem (Abshire et al., 2000) the filters are low-pass circuit with 3-dB attenuation bandwidths and impulse response pulse shapes closely approximated by Gaussian functions. The optimal filter is a low-pass filter with the integration time equal to the echo pulse width (Koskinen et al., 1992). In order to accommodate the wide variability in the spreading of echo pulses a multiple channel receiver will be considered and
- to reduce the probability of false alarm (P_{FA}), a range gate interval (T_{RG}) is used which allows the detected signal to pass the discriminator only during an interval over which the return pulse from the ground is expected to arrive.

Moreover, we assume the ground target is diffuse (lambertian surface scattering model) and there are no specular reflections. Table 9 reports the value of main parameters used in performance analysis.

4.1. APD output statistics

The probability density function $p(x|\bar{n})$ which describes the signal x at the output of APD, for a given average number $\bar{n}$ of detected primary photons over the integration interval can be written as (Koskinen et al., 1992; Sun et al., 1992)

$$p(x|\bar{n}) = \sum_{m=0}^{\infty} p(x|m)P(m|\bar{n}), \tag{1}$$

where $p(x|m)$ is the conditional probability density of circuit noise (pre-amplifier and APD surface leakage current), $P(m|\bar{n})$ is the conditional probability of observing m secondary photoelectrons in response to $\bar{n}$ detected primary photoelectrons (with $m \geqslant \bar{n}$ and $\bar{n} > 0$).

In Eq. (1) the function $p(x|m)$ can be considered as

$$p(x|m) = \frac{1}{\sqrt{2\pi\sigma^2}} \exp\left[-\frac{(x-\bar{x}_m)^2}{2\sigma^2}\right] \tag{2}$$

with mean and variance given by

$$\bar{x}_m = m + \frac{I_S \tau}{eG},$$

$$\sigma^2 = \frac{I_a^2 \tau}{e^2} + \frac{I_S \tau}{eG},$$

where I_S is the APD leakage noise current (A), τ the filter response width (s), e the electron charge (C), G the APD gain, I_a the preamplifier noise current (A/Hz$^{1/2}$).

Table 9
Value of main parameters used in LAPE performance model

Parameter	Symbol	Value
BepiColombo mission parameters		
Solar spectral irradiance at Mercury surface ($W m^{-2} nm^{-1}$)	I_{sun}	0 (nightlight conditions) 6.8 (daylight, worst conditions)
Absolute temperature of Mercury (K)	T	95 (nightlight conditions) 688.5 (daylight conditions)
Surface reflectivity (%)	ρ	10 (nightlight conditions) 5 (daylight conditions)
TXU parameters		
Laser transmitter's energy/pulse (mJ)	E_t	80
Laser pulse width (ns)	σ_t	10
Laser wavelength (nm)	λ	1064
Laser beam divergence (mrad)	θ	0.2
Optics transmittance	η_{TX}	0.9
RXU parameters		
Receiver transmission	η_{RX}	0.85
Receiver field of view (mrad)	θ_{FOV}	0.4
Receiver area (m^2)	A_R	0.0491
Interference filter receiver bandpass (nm)	$\Delta\lambda_f$	3
Interference filter transmittance	η_f	0.625
Detector parameters		
APD quantum efficiency	η_{APD}	0.40
Dark current (A)	I_d	10e−12
Noise current ($A/Hz^{0.5}$)	I_n	1e−12
APD gain	G	100
Ionization coefficient ratio	k_{eff}	0.008
Excess noise factor	$F = k_{eff}G + (2 - 1/G)(1 - k_{eff})$	2.77

Simple expression for conditional probability $P(m|\bar{n})$ has been derived by Webb et al. (1974):

$$P(m|\bar{n}) = \frac{1}{\sqrt{2\pi\bar{n}G^2F}\left(1+\frac{m-\bar{n}G}{\bar{n}GF/(F-1)}\right)^{3/2}} \times \exp\left(-\frac{(m-\bar{n}G)^2}{2nG^2F\left(1+\frac{m-\bar{n}G}{\bar{n}GF/(F-1)}\right)}\right), \quad (3)$$

where F is the excess noise factor.

According to the Webb approximation (3), the conditional density probability in presence of background photons only is

$$p_b = P(m|\bar{n} = \bar{n}_b), \quad (4)$$

where $\bar{n}_b$ is the number of background photons absorbed by the APD.

While the conditional density probability in presence of signal and background photons is

$$p_{sb} = P(m|\bar{n} = \bar{n}_s + \bar{n}_b), \quad (5)$$

where $\bar{n}_s$ is the number of signal photons absorbed by the APD.

To evaluate expressions (4) and (5) $\bar{n}_s$ and $\bar{n}_b$ have to be calculated since G and F are characteristic parameters of APD manufacturer provided.

The number of signal photoelectrons generated per pulse is (Cheng et al., 2000)

$$\bar{n}_s = \frac{E_t}{h\nu}\frac{\rho}{\pi}\frac{A_R}{R^2}\eta_{RX}\eta_{APD}\eta_{TX}\eta_f, \quad (6)$$

where E_t is the transmitted laser pulse energy (J), $h\nu$ the photon energy (J), ρ the albedo, A_R the receiving area (m^2), R the range from target (m^2), η_{RX} the receiver transmission, η_{APD} the APD quantum efficiency, η_{TX} the optics transmittance, η_f the interference filter transmittance.

Following again the analysis of Cheng et al. the total number of background photons can be written as

$$\bar{n}_b = \left(\lambda_{Sun} + \lambda_{Mer} + \frac{I_D}{e}\right)\tau, \quad (7)$$

where λ_{Sun} is the number of solar background photoelectron per second (s^{-1}), λ_{Mer} the Mercury radiation photon rate (s^{-1}), I_D the APD dark current (A).

The number of solar background photoelectron rate λ_{Sun} is (Cheng et al., 2000)

$$\lambda_{Sun} = \frac{I_{Sun}}{h\nu}\frac{\rho}{\pi}A_R\pi\left(\frac{\theta_{FOV}}{2}\right)^2\eta_{RX}\eta_{APD}\eta_f\Delta\lambda_f, \quad (8)$$

where I_{Sun} is the solar irradiance ($W m^{-2} nm$), θ_{FOV} the receiver field of view (rad), $\Delta\lambda_f$ the interference filter bandpass (nm).

In the developed model to analyse LAPE performance the parameter λ_{Sun} will be set to zero in night light condition.

Mercury radiation photon rate λ_{Mer} can be written as

$$\lambda_{Mer} = \frac{W}{\pi h\nu}A_R\pi\left(\frac{\theta_{FOV}}{2}\right)^2\eta_{RX}\eta_{APD}\eta_f\Delta\lambda_f, \quad (9)$$

where W is the spectral radiant emittance of a blackbody (Mercury) for a wavelength λ and absolute temperature T

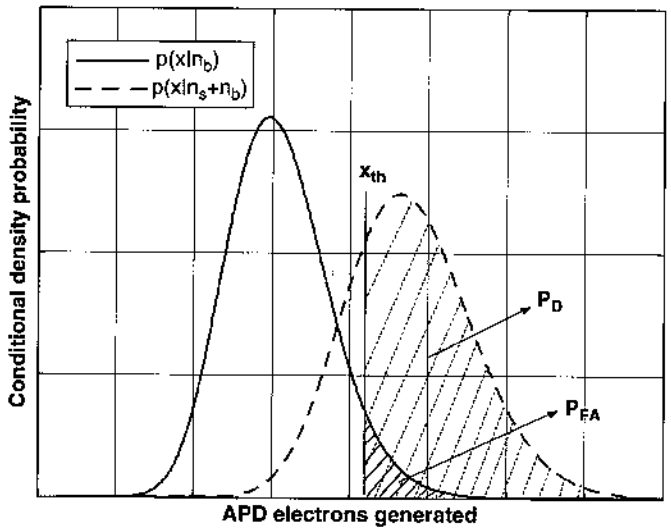

Fig. 6. Model of conditional density probability in presence of background photons only (solid line) and conditional density probability in presence of signal and background photons (dashed line) versus APD electrons generated.

given by

$$W = \frac{2\pi hc^2}{\lambda^5}\frac{1}{e^{ch/\lambda KT}-1}, \tag{10}$$

where h is the Plank's constant (J s), K the Boltzmann's constant ($J K^{-1}$), c the velocity of light in vacuum ($m s^{-1}$).

4.2. Probability of detection and probability of false alarm

Our model predicts LAPE single-shot detection probability P_D and probability of false alarm P_{FA}, which is the probability that the receiver noise will exceed the threshold and generate a false measurement of TOF. To evaluate P_D, P_{FA} and the threshold we used Eq. (1) in the Neyman–Pearson method.

Fig. 6 shows an example of the function $p(x|n_b)$ and $p(x|n_b+n_s)$[1] versus x (APD electrons generated).

Using Eqs. (1), (2), (4) and (5) P_{FA} and P_D can be written as

$$P_{FA} = \int_{x_{th}}^{+\infty} p(x|n_b)\,dx = \int_0^{+\infty} P(m|n_b)\,dm \int_{x_{th}}^{+\infty} p(x|m)\,dx, \tag{11}$$

$$P_D = \int_{x_{th}}^{+\infty} p(x|n_b+n_s)\,dx = \int_0^{+\infty} P(m|n_b+n_s)\,dm \int_{x_{th}}^{+\infty} p(x|m)\,dx, \tag{12}$$

where x_{th} is the threshold.

With the Neyman–Pearson method the P_{FA} is set to a fixed value and the threshold is consequently evaluated.

[1]From now in the following equations $\bar{n}_s = n_s$ and $\bar{n}_b = n_b$.

The approach described for estimation of P_D and P_{FA} is known as "*near exact analysis*". Previous studies demonstrate that approximate forms of APD output photoelectron distribution must be used since the exact distribution given by Eq. (1) requires an excessive amount of computation time in numerical calculation of P_D and P_{FA} (Sun et al., 1992 and works referenced there). Following Cheng et al. performance analysis of NLR (Cheng et al., 2000), it is possible to evaluate integrals (11) and (12) by numerical quadrature with acceptable computation time. Cheng applies a smart changing of variable in the conditional probability density function of circuit noise $p(x|m)$ (Eq. (2)) and in the Webb's approximation (Eqs. (4) and (5)).

If in the integral of function $p(x|m)$ in (2) the variable t is set as

$$t = \frac{x - m - (I_S\tau/eG)}{\sqrt{2}\sigma}$$

and considering the following definition for erfc:

$$\mathrm{erfc}(t) = \frac{2}{\sqrt{\pi}}\int_{t_{th}}^{+\infty} e^{-t^2}\,dt$$

we have that

$$\int_{x_{th}}^{+\infty} p(x|m)\,dx = \frac{1}{2}\,\mathrm{erfc}\left(\frac{x_{th} - m - (I_S\tau/eG)}{\sigma}\right). \tag{13}$$

If in the function $P(m|\bar{n})$ the variable z is set as

$$z = \frac{m - \bar{n}G}{\sqrt{\bar{n}G^2F}} \tag{14}$$

replacing (14) in (3) and considering expressions (4) and (5) respectively, for p_b and p_{sb} and the result (13), integrals (11) and (12) can be written as

$$P_{FA} = \frac{1}{2}\int_{-n_bG/\sigma_b}^{+\infty} dz\,P(z|n_b)\,\mathrm{erfc}\left(\frac{x_{th} - \sigma_b z - n_bG - I_s\tau/Ge}{\sigma}\right), \tag{15}$$

where

$$P(z|n_b) = \frac{1}{\sigma_b\sqrt{2\pi}\left[1+\frac{G(F-1)}{\sigma_b}z\right]^{3/2}} \times \exp\left[-\frac{z^2}{2\left(1+\frac{G(F-1)}{\sigma_b}z\right)}\right],$$

$$\sigma_b = \sqrt{\bar{n}_bG^2F},$$

while

$$P_D = \frac{1}{2}\int_{-(n_s+n_b)G/\sigma_{sb}}^{+\infty} dz\,P(z|n_s+n_b) \times \mathrm{erfc}\left(\frac{x_{th} - \sigma_{sb}z - (n_s+n_b)G - I_s\tau/eG}{\sigma}\right), \tag{16}$$

where

$$P(z|n_s+n_b)=\frac{1}{\sigma_{sb}\sqrt{2\pi}\left[1+(G(F-1)/\sigma_{sb})z\right]^{3/2}}\times\exp\left[-\frac{z^2}{2(1+(G(F-1)/\sigma_{sb})z)}\right],$$

$$\sigma_{sb}=\sqrt{(\bar{n}_s+\bar{n}_b)G^2F}.$$

4.3. Echo pulse width

The reflected laser pulse is distorted by surface features within the laser footprint so that the shape of the received waveform contains important information about roughness, slope, and reflectivity. The centroid of the backscattered pulse is the mean round-trip TOF range to surface within the laser footprint, weighted by the reflectivity and areal extent of the lighted surface patch. Gardner developed analytic expressions for received pulse width σ_p. In particular the expression for mean square detected pulse width σ_p^2 adapted for nadir pointing is (Gardner, 1992)

$$\sigma_p^2=(\sigma_l^2+\sigma_h^2)+\frac{4\mathrm{Var}(\Delta\xi)}{c^2}$$

system effects + roughness effects

$$+\frac{4R^2\tan^2\theta}{c^2}(\tan^2\theta+\tan^2 S)$$

+ beam curvature and slope effects, (17)

where σ_l is the rms laser pulse width (s), $\sigma_h=(\tau/2\sqrt{2\ln 2})$ the rms width of receiver impulse response (s) with τ low-pass filter impulse width (Abshire et al., 2000), $\Delta\xi$ the surface roughness, θ the laser beam divergence angle (rad), S the surface slope (rad).

Using the analytical expression (17) the broadening effects on the echo pulse due to laser effect σ_h, surface roughness, beam curvature and surface slope have been estimated for different heights (from 300 to 1500 km), variance of surface roughness (1, 4 and 6 m) and surface slope (in the range 0°–45°). The width of receiver impulse response σ_h is considered null (ideal receiver). Fig. 7 shows the results for $\mathrm{Var}(\Delta\xi)=4$ m while Table 10 reports the echo pulse width at 0° and 45° for different values altitude and for $\mathrm{Var}(\Delta\xi)=1$, 4, 6 m.

The analysis performed varying the surface roughness shows that for low values of slope surface (less than 10°) the echo pulse width σ_p is almost independent of the altitude and strongly depends on roughness value, while for higher surface slopes the σ_p value is independent of roughness value and for a same slope, it varies with the altitude.

4.4. False alarm rate and range gate time interval

The false alarm rate has been defined as

$$n_{FA}=P_{FA}\frac{T_{RG}}{\tau}, \quad (18)$$

where T_{RG} is the range gate time interval (s), τ the filter response width (s).

Following MOLA receiver subsystem (Abshire et al., 2000) also in LAPE the receiver threshold levels are automatically and independently adjusted in order to

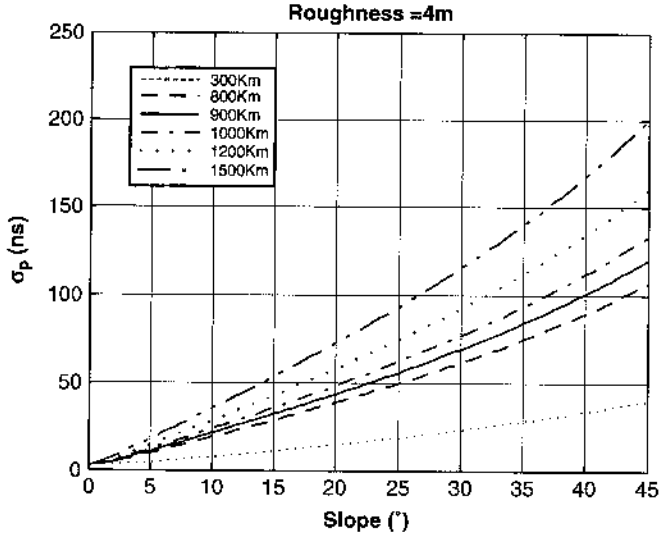

Fig. 7. Echo pulse width σ_p (with $\sigma_h=0$) versus surface slope S for variance roughness 4 m and different values of range to surface R.

Table 10
Values of echo pulse width σ_p (with $\sigma_h=0$) for $S=0°$ and $S=45°$ at different values of altitude R and for roughness 1, 4, 6 m

Range (km)	$\sigma_p(S=0°)$ (ns)	$\sigma_p(S=45°)$ (ns)
$\mathrm{Var}(\Delta\zeta)=1$ m; $\sigma_h=0$		
1500	12.038	2001.4
1200	12.036	1601.2
1000	12.034	1334.3
900	12.304	1200.9
800	12.033	1067.5
300	12.032	400.46
$\mathrm{Var}(\Delta\zeta)=4$ m; $\sigma_h=0$		
1500	28.504	2001.6
1200	28.503	1601.4
1000	28.503	1334.6
900	28.503	1201.2
800	28.502	1067.5
300	28.502	401.29
$\mathrm{Var}(\Delta\zeta)=6$ m; $\sigma_h=0$		
1500	41.263	2001.8
1200	41.262	1601.6
1000	41.262	1334.9
900	41.262	1201.5
800	41.262	1068.2
300	41.261	402.40

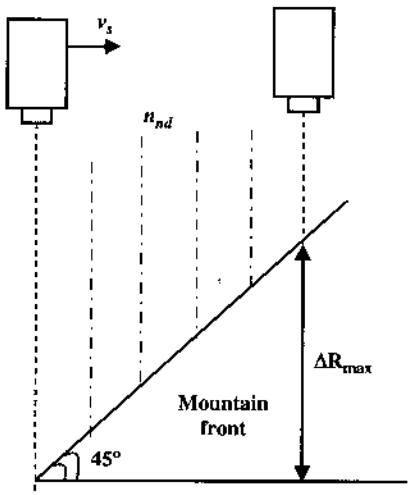

Fig. 8. Sketch to simulate the echo pulse in order to evaluate the range gate time interval T_{RG}. The dotted lines are for successful range to surface measurement, the dashed-dotted lines for missed detections (n_{nd}). The sub-satellite point velocity is v_s, and ΔR_{max} is the useful distance range after n_{nd} non-detection.

maintain a false alarm rate of approximately 1% per receiver channel.

In order to evaluate a suitable value for range gate time interval, T_{RG}, we used the following formula:

$$T_{RG} = \left(\frac{2\Delta R_{max}}{c}\right)2 + \sigma_p^{max}, \tag{19}$$

where (see Fig. 8), ΔR_{max} is the useful distance range after n_{nd} non-detections, n_{nd} the number of possible consecutive non-detections (range measurement signals which does not cross the discriminator threshold), σ_p^{max} the echo pulse width for maximum value of altitude ($R = 1200$ km) and slope ($S = 45°$) and roughness ($\mathrm{Var}(\Delta\zeta) = 6$ m).

Eq. (19) takes also in account that the signal could be backscattered from a slope ascent or descent.

We simulate receiving the echo pulse from a mountain front with a surface slope of 45° (maximum value), to miss n_{nd} consecutive backscattered pulses (dashed-dotted lines in Fig. 8) and then to measure the range to surface again (dotted line again in Fig. 8).

The useful distance range ΔR_{max} can be written as

$$\Delta R_{max} = \frac{v_s}{PRF}\tan 45°(n_{nd} + 1), \tag{20}$$

where v_s is the 2.5 km/s sub-satellite point velocity, PRF the 16 Hz pulse repetition frequency, 45° the maximum estimated dip angle on Mercury surface, n_{nd} the 4 number of possible consecutive non-detections, σ_p^{max} the 1601.6 ns echo pulse width for $R = 1200$ km (goal altitude), $S = 45°$ and $\mathrm{Var}(\Delta\zeta) = 6$ m (see Table 10).

Replacing (20) in (19) we have $T_{RG} \cong 12\,\mu$s.

4.5. Signal-to-noise ratio

Laser altimeter signal strength depends on laser pulse power backscattered from the target surface and collected by the receiver telescope. Competing processes are optical shot noise, background noise, detector noise and pre-amplifier noise.

If the background is assumed to be constant, or more specifically, if the fluctuation of the background intensity is not at frequencies that fall within the bandwidth of the post-detection filter, for nadir-viewing altimetry operation, the ratio of signal power to noise power at the output of the interference filter, which follows the APD, is

$$\mathrm{SNR} = \frac{I_S^2}{I_N^2} = \frac{G^2 I_{SD}^2}{I_{NS}^2 + I_{NB}^2 + I_{ND}^2 + I_A^2 B}, \tag{21}$$

where I_S is the signal current from APD (A), I_N the noise current (A), $I_{SD} = en_s/\sigma_p$ the signal current impinging on detector (A) with n_S given by Eq. (6) and σ_p received pulse width (s) given by Eq. (17), $I_{NS}^2 = 2eBI_{SD}FG^2$ the noise signal current (A), $I_{NB}^2 = 2eBI_BFG^2$ the noise background current (A) with $I_B = e(\lambda_{Sun} + \lambda_{Mer})$ the background current given by Eqs. (8) and (9), I_A the APD noise current (A/Hz$^{1/2}$), $I_{ND}^2 = 2eI_DB$ with I_D APD dark current (A) (Perkin Elmer, 2001), B the detection bandwidth (Hz).

Replacing in (21) the previous equations, the SNR can be rewritten as

$$\mathrm{SNR} = \frac{G^2(en_S/\sigma_p)^2}{2eBFG^2[e(\lambda_{Sun} + \lambda_{Mer}) + en_S/\sigma_p] + 2eBI_D + I_A^2 B}, \tag{22}$$

which is the expression for SNR implemented in the developed software for LAPE performance analysis.

4.6. Ranging resolution

Ranging measurement resolution in the TOF single-shot laser altimetry technique is inversely proportional to SNR due to the timing uncertainty with a fixed threshold level. The signal variation results in a range error R_r that can be estimated from the expression (Bufton, 1989; Koskinen et al., 1992; Abshire et al., 2000):

$$R_r = \frac{c\sigma_p}{2\mathrm{SNR}}, \tag{23}$$

where σ_p is the echo pulse width given by Eq. (17), SNR is SNR Ratio given by Eq. (22).

5. LAPE performance in nightlight conditions

For night light conditions we consider the following parameters setting:

- temperature of Mercury $T = 95$ K (ESA, 2002),
- solar spectral irradiance at Mercury surface $I_{Sun} = 0$,
- solar background photoelectron rate $\lambda_{Sun} = 0$ (Eq. (8)),
- surface reflectivity of 10% (ESA, 2003) and
- false alarm rate equal to 0.01.

5.1. Nightlight detection probability and low-pass filters setting

In order to verify in which conditions LAPE satisfies the requirements proposed by ESA for probability of detection P_D versus range to surface R (ESA, 2003), we apply the expressions (15), (16) and (18) to evaluate P_D versus slope surface S, for different values of R (from 300 to 1500 km) and at variance surface roughness of 4 m. The result is showed in Fig. 9 with a table after the graph to help the analysis. The table reports in first column the ESA requirements for P_D for the provided altitudes: 800–900–1000–1200 km, in second column the slope surface values to satisfy the previous requirements. The requirements individuate a range of surface slope from 3.7° (at 1200 km with $P_D \geqslant 40\%$) to 11.1° (at 800 km with $P_D \geqslant 95\%$). Therefore the requirements proposed by ESA are satisfied for particular surface slope ranges and for increasing values of altitude these ranges decreasing.

The graph in Fig. 9 are obtained setting in the integrals (15) and (16) (and in analytical expression for n_b Eq. (7))

$$\tau = \sqrt{\sigma_p^2 - \sigma_h^2},$$

that is we are considering an ideal case where the low-pass filter impulse width τ is always equal to the echo pulse width and neglecting the receiver impulse response contribution σ_h. Starting from this position a finite number of filter widths have been fixed.

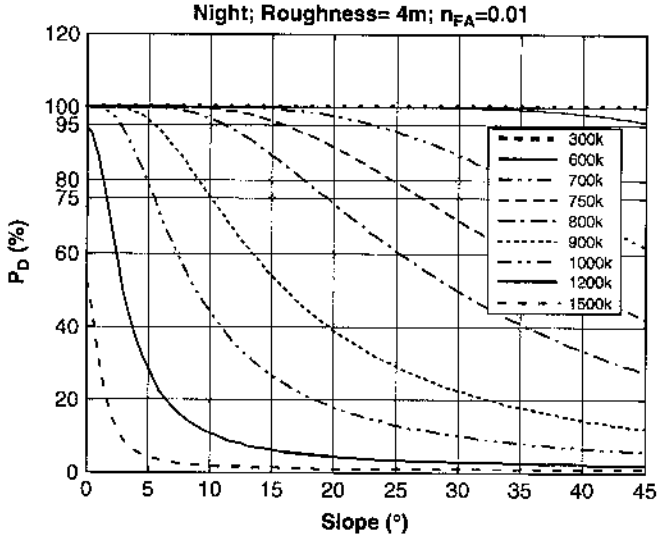

Night; Var(Δζ)=4m			
ESA requirements P_D @ R (km)	Slope	σ_p (with σ_h=0)	P_{FA} value
>95% @ 800	≤11.1°	211e-9	1.76e-4
>75% @ 900	≤10.2°	215e-9	1.79e-4
>60% @ 1000	≤7.4°	174e-9	1.45e-4
>40% @ 1200 (goal)	≤3.7°	109e-9	0.9e-4

Fig. 9. Probability of detection P_D versus slope to surface S for $n_{FA} = 0.01$, for roughness variance $\mathrm{Var}(\Delta\zeta) = 4$ m and range to surface R from 300 to 1500 km in nightlight conditions. The table reports the value of required ESA P_D (ESA, 2003), the slope values where the requirement is fulfilled, the echo pulse width at that slope and the correspondent P_{FA} value (Eq. (15) with $\tau = \sqrt{\sigma_p^2 - \sigma_h^2}$).

Taking into account the results of Fig. 9, the echo pulse widths (Fig. 7) for the surface slope values, which fulfil the requirements on P_D, have been estimated. The values obtained have been considered as the low-pass filter impulse widths, τ. The results are reported in third column of the table of Fig. 9. In order to assure that also the largest echo pulse (for $R = 1200$ km and $S = 45°$) is detected by the LAPE receiver subsystem, in addition to the indicated four low-pass filters, we considered also a fifth filter with impulse response width equal to 2 μs. The minimum value of 109 ns for the filters could appear a choice rather conservative relatively a typical case of flat surface, but as of this writing the geological characteristics of Mercury are not well known and the choice depends on described theoretic estimation of σ_p.

In conclusion in our model the LAPE receiver subsystem contains also a parallel bank of five low-pass filters (five-pole Bessel design) with τ impulse response width 109–174–211–215 ns and 2 μs. Following the MOLA receiver subsystem, when an echo pulse is received the filter (channel) with the closest matching response width to the echo stops the range counter. It is important to note that the low-pass filters spread the pulse but preserve the pulse energy.

5.2. Nightligth SNR and ranging resolution evaluation

Using expression (22) the SNR of LAPE versus surface slope, in range 0°–45°, and for different heights R and surface roughness, has been studied. The detection bandwidth B is (Abshire et al., 2000):

$$B = \frac{1/\sqrt{\sigma_p^2 - \sigma_h^2}}{3} = \frac{1/\tau}{3},$$

where τ is the filter impulse response width. B ranges from 0.2 MHz ($\tau = 2$ μs) to 3 MHz ($\tau = 109$ ns). The ranging resolution R_r has been estimated from the value of the SNR using the expression (23). Ranging resolution as a function of surface slope has been analysed varying the range to surface from 300 to 1500 km. Based on the ESA requirements for nightlight conditions the ranging resolution at 1000 km has to be less than 1 m (ESA, 2003). The performed analysis shows that the ranging resolution does not depend on the surface roughness value. The results for SNR and R_r are reported in Fig. 10.

R_r is less than 1 m at 1000 km for a surface slope $S < 6.5°$. Decreasing the altitude the ranging resolution improves and the condition $R_r < 1$ m is satisfied for higher surface slope ranges.

6. LAPE performance in daylight conditions

For daylight conditions we consider the following parameter setting:

- day temperature of Mercury $T = 688.5$ K (ESA, 2002),

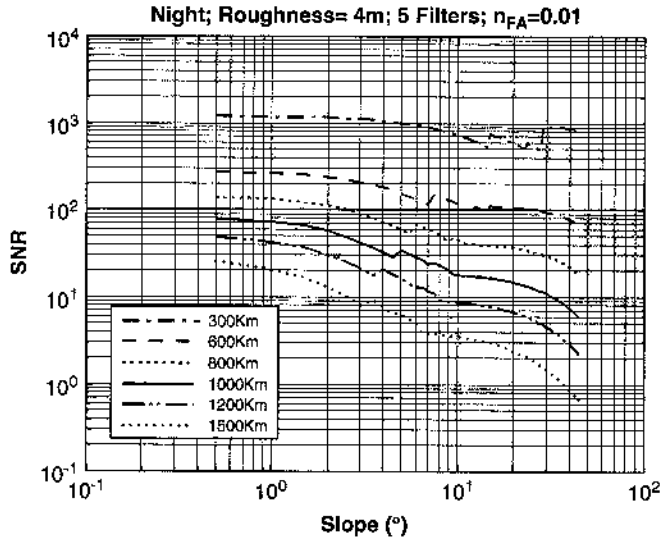

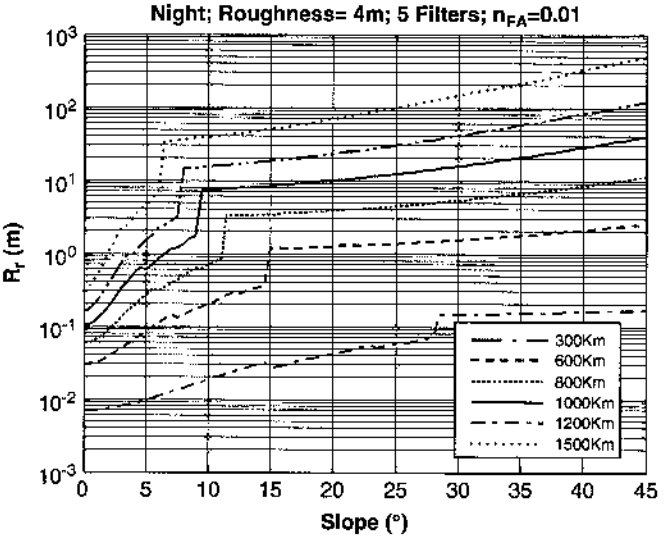

Fig. 10. LAPE signal-to-noise ratio (SNR) and ranging resolution R_r versus surface slope S, for different heights R and for variance roughness of 4 m in nightlight conditions. The LAPE receiver subsystem includes 5 low-pass filters—see paragraph (5.1).

- solar spectral irradiance at Mercury surface $I_{Sun} = 6.8\,W\,m^{-2}\,nm^{-1}$,
- surface reflectivity of 5% (ESA, 2003) and
- false alarm rate equal to 0.01.

6.1. Daylight detection probability

Also for daylight condition we verify if the designed laser altimeter satisfies the ESA requirements on P_D versus range to surface R (ESA, 2003), applying again Eqs. (15), (16) and (18) to analyse LAPE P_D as a function of range to surface R, for different surface slope (from 0° to 45°). The variance surface roughness is 4 m. The obtained results in Fig. 11 show that the proposed requirements are not verified. Nevertheless it has to be noted that the low values of detection probability achieved in daylight condition are compensated by the low value of false alarm rate set to 1%

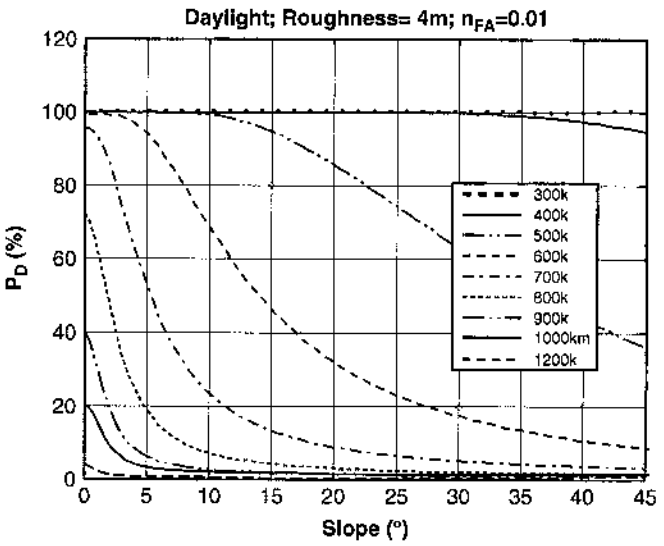

ESA requirements P_D @ R	Max P_D achieved for S=0°
P_D>70% @ 800km (goal)	40%
P_D>50% @ 900km] (goal)	17%
P_D>40% @ 1000km (goal)	7%

Fig. 11. Probability of detection P_D versus range to surface R and slope to surface S for $n_{FA} = 0.01$, for roughness variance $Var(\Delta\zeta) = 4\,m$ in daylight conditions. The table reports the value of required P_D provided by ESA (ESA, 2003) and the maximum value of P_D for $S = 0°$.

per receiving channel and that for an altitude less than 500 km LAPE detects the backscattered signal with P_D higher than 90% and in a surface slope range values up to 10°.

As for nightlight conditions also the graph in Fig. 11 is obtained considering an ideal case where the low-pass filter impulse width τ is always equal to the echo pulse width (or the width of receiver impulse response $\sigma_h = 0$). No remarkable improvements for P_D have been obtained in our simulations considering the five low-pass filter in RXU.

6.2. Daylight SNR and ranging resolution evaluation

Taking into account the analysis of SNR and ranging resolution obtained in nightlight conditions, we analysed the LAPE performance in daylight conditions with the same five low-pass filters (paragraph 5.1) and for variance surface roughness of 4 m. In order to satisfy the ESA requirements for daylight conditions the ranging resolution R_r at 1200 km has to be less than 2 m (ESA, 2003).

Fig. 12 shows the results of SNR and ranging resolution R_r as function of surface slope for variance roughness 4 m.

The requirement R_r is less than 2 m at 1200 km for a surface slope $S < 1.8°$. Decreasing the altitude the ranging resolution improves and the condition $R_r < 2$ m is satisfied for larger surface slope ranges.

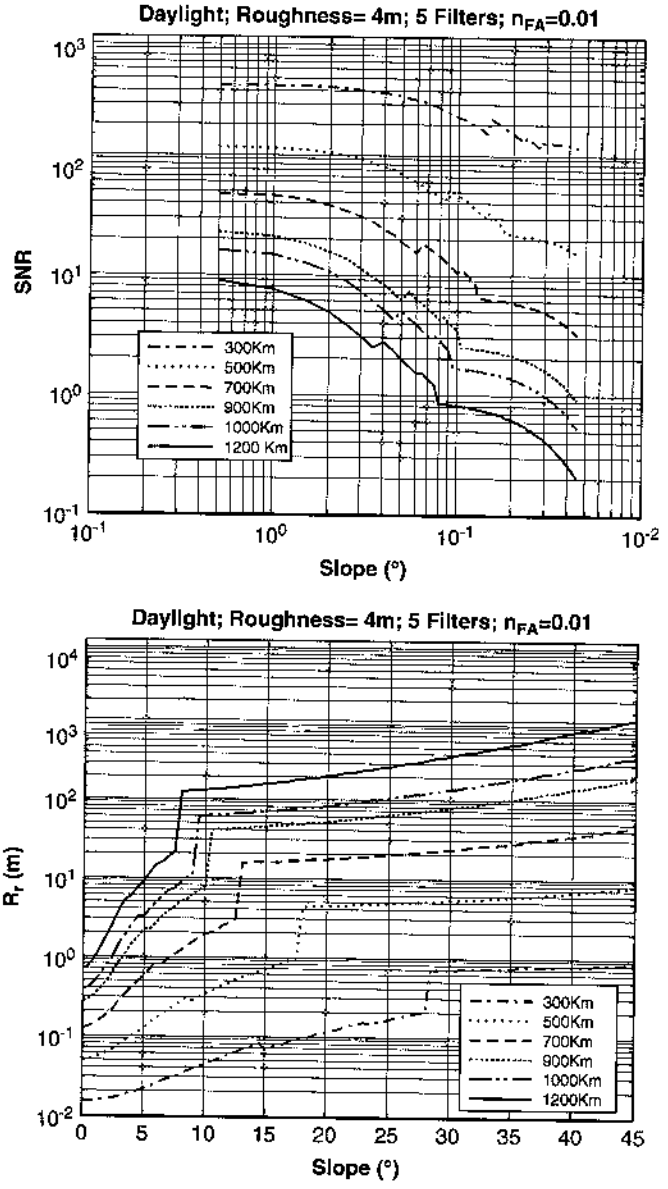

Fig. 12. LAPE signal-to-noise ratio (SNR) and ranging resolution R_r versus surface slope S for different heights and for variance roughness 4 m in daylight conditions. The LAPE receiver subsystem includes 5 low-pass filters—see paragraph (5.1).

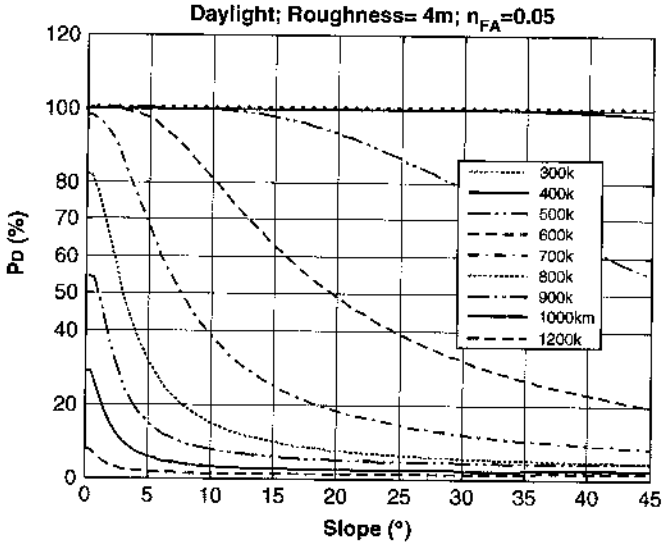

Day; Var(Δζ)=4m	
P_D @ R (km)	Slope range
>70% @ 800 (goal)	≤ 1.5°
>50% @ 900 (goal)	≤ 0.7°
>40% @ 1000 (goal)	NF

Fig. 13. Probability of detection P_D versus range to surface R and slope to surface S for $n_{FA} = 0.05$, for roughness variance $\mathrm{Var}(\Delta\zeta) = 4\,\mathrm{m}$ in daylight conditions. The table reports the ESA requirements for P_D (ESA, 2003). NF is for Not Fulfilled.

7. Increment of false alarm rate value

In order to improve the LAPE performance in daylight conditions we increased the false alarm rate value n_{FA} (Eq. (18)) starting from the fixed value of 1% per channel. This means an higher number of false alarm (or an higher probability of false alarm since the range gate time interval T_{RG} and the filter response width τ are constant), but also an higher probability of detection (see Fig. 6). Setting $n_{FA} = 5\%$, Fig. 13 shows the obtained result for probability of detection.

Respect to the performance with $n_{FA} = 1\%$ (Fig. 11 and Fig. 12) the requirement on probability of detection are fulfilled also for an altitude of 900 km and in a slope surface range slightly wider. The requirement on ranging resolution R_r is satisfied in the same surface slope range (see Section 5.2).

Simulations with a further increasing of the false alarm rate from 5% to 10% did not show satisfactory improvements in term of slope surface range measurements.

In order to complete LAPE performance analysis we simulated also the instrument response in night conditions with $n_{FA} = 5\%$. The results in for detection probability are showed in Fig. 14. The performance simulation did not show improvements in terms of ranging resolution respect to the performance with $n_{FA} = 1\%$.

8. Conclusions

Preliminary design and performance analysis of a laser altimeter for planetary exploration (LAPE) have been described. A low-technological risk approach has been adopted, and the reference scenario of the BepiColombo mission to Mercury is considered. Design and specifications of the LAPE units are described separately, as well as budgets and operational strategy. Then, performance is evaluated under different operative conditions (nighttime or daylight) and terrain features (slope and roughness). Results show that with the adopted design and measurement approach, mission requirements are fulfilled over a large interval of surface slopes and from the maximum

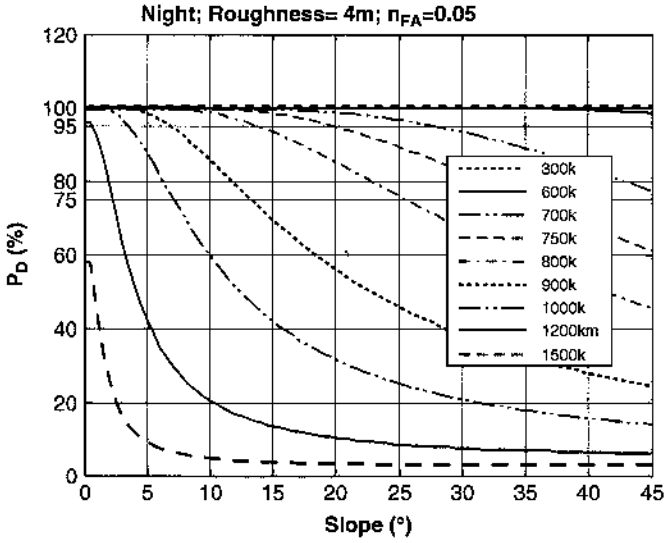

Night; Var(Δζ)=4m	
Required P_D @ R (km)	Slope range
>95% @ 800	<13.8°
>75% @ 900	<13.2°
>60% @ 1000	<9.9°
>40% @ 1200 (goal)	≤5.3°

Fig. 14. Probability of detection P_D versus range to surface R and slope to surface S for $n_{FA} = 0.05$, for roughness variance $\mathrm{Var}(\Delta\zeta) = 4$ m in night conditions. The table reports the ESA requirements for P_D (ESA, 2003) and the slope range where the requirement is fulfilled.

requested altitude for night operations, while in presence of Sun irradiance operations will be restricted around the periapsis. This is largely due to the harshness of the selected operational environment (around Mercury) that is very close to the Sun itself. However, the performance model demonstrates that the proposed instrument design is capable to exploit high performance at higher altitudes than its predecessors (Clementine, NLR, Mola) with a lower total mass.

Acknowledgments

The authors would like to thank Prof. Luciano Iess (from Dipartimento di Ingegneria Aerospaziale e Aeronautica of University of Rome "La Sapienza") for his valuable contribution to the scientific aspects of the study.

This work was funded by the European Space Agency (ESA) under ESA/ESTEC Contract No. 17080/03/NL/HB, in the context of the BepiColombo assessment activities.

References

Abshire, J.B., Sun, X., Afzal, R.S., 2000. Mars Orbiter Laser Altimeter: receiver model and performance analysis. Appl. Opt. 39 (15), 2449–2460.

Bufton, J.L., 1989. Laser Altimetry Measurements from Aircraft and Spacecraft. Proc. IEEE 77 (3), 463–476.

Cheng, A.F., Cole, T.D., Zuber, M.T., Smith, D.E., Guo, Y., Davidson, F., 2000. In-flight calibration of the Near Earth Asteroid Rendezvous Laser Rangefinder. Icarus 148, 572–586.

Cole, T.D., 1998. NEAR Laser Rangefinder: a tool for the mapping and topologic study of asteroid 433 Eros. John Hopkins Appl. Tech. Digest 19 (2).

ESA, 2000. BepiColombo. An interdisciplinary Cornerstone Mission to the Planet Mercury. System and Technology Study Report, April.

ESA, 2002. Mercury Environmental Specification—Part 1. Issue 2, July.

ESA, 2003. Annex 1/B. LAPE Technical Requirements—Phase 2&3. Issue 02, rev.02.

Forrester, P.A., Hulme, K.F., 1981. Laser Rangefinder. Opt. Quant. Electron. 13.

Gardner, S.C., 1992. Ranging performance of satellite laser altimeters. IEEE Trans. Geosci. Remote Sensing 30 (5).

Garvin, J.B., Bufton, J.L., Blair, J.B., Harding, D., Luthcke, S.B., Frawley, J.J., Rowlands, D.D., 1998. Observations of the Earth's topography from the Shuttle Laser Altimeter (SLA): laser pulse echo recovery measurements of terrestrial surfaces. Phys. Chem. Earth 23, 1053–1068.

Harding, D.J., Bufton, J.L., Frawley, J.J., 1994. Satellite Laser Altimetry of Terrestrial Topography: vertical accuracy as a function of surface slope, roughness, and cloud cover. IEEE Trans. Geosci. Remote Sensing 32 (2).

Koskinen, M., Kostamovaara, J., Myllilla, R., 1992. Comparison of the continuos wave and pulsed time-of-flight laser rangefinding techniques: optics, illumination and image sensing for Machine Vision VI. Proc. SPIE 1614, 296–305.

Krebs, D.J., Novo-Gradac, A.M., Li, S.X., Lindauer, S.J., Afzal, R.S., Yu, A.W., 2005. Compact, passively Q-switched Nd:YAG laser for the MESSENGER mission to Mercury. Appl. Opt. 44 (9), 1715–1718.

Margot, J.L., Campbell, D.B., Jurgens, R.F., Slade, M.A., 1999. The topography of Tycho crater. J. Geophys. Res. 104, 875–882.

Mattei, S., Santovito, M.R., Moccia, A., 2006. Laser altimeter for microsatellite: a feasibility study. IEEE Trans. Aerospace Electron. Syst. 42, 4.

Murphy, E., Rando, N., Falkner, P., Peacock, T., 2003. LAPE Laser Altimeter for Planetary Exploration. SPIE, vol. 5240. In: Proceedings of 10th Symposium International on Remote Sensing, Barcelona (Spain), September 8–12, 2003.

Neukum, G., Oberst, J., Hoffmann, H., Wagner, R., Ivanov, B.A., 2001. Geologic evolution and cratering history of Mercury. Planet. Space Sci. 49, 1507–1521.

Neumann, G.A., Rowlands, D.D., Lemoine, F.G., Smith, D.E., Zuber, M.T., 2001. Crossover analysis of Mars Orbiter Laser Altimeter data. J. Geophys. Res. 106, 753–768.

Nozette, S., et al., 1994. The Clementine mission to the Moon: scientific overview. Science 266, 1835–1839.

Perkin Elmer, 2001. Avalanche Photodiodes: A User's Guide. Technical Note.

Robinson, M.S., Lucey, P.G., 1997. Recalibrated Mariner 10 color mosaics: implications for mercurian volcanism. Science 275, 197–200.

Smith, D.E., Zuber, M.T., Neumann, G.A., Lemoine, F.G., 1997. Topography of the Moon from the Clementine lidar. J. Geophys. Res. 102, 1591–1611.

Solomon, S.C., et al., 2001. The MESSENGER mission to Mercury: scientific objectives and implementation. Planet. Space Sci. 49, 1445–1465.

Sun, X., Davidson, F.M., Boutsikaris, L., Abshire, J.B., 1992. Receiver characteristics of laser altimeters with avalanche photodiodes. IEEE Trans. Aerospace Electron. Syst. 28 (1).

Sun, X., Cavanaugh, J.F., Smith, J.C., Bartels, A.E., 2004. Mercury Laser Altimeter. Instrument design, testing, and performance verification. In: Proceedings of the 22nd ILRC 2004, Matera (Italy), July 12–16, 2004.

Watters, T.R., Cook, A.C., Robinson, M.S., 2001. Large-scale lobate scarps in the southern hemisphere of Mercury. Planet. Space Sci. 49, 1523–1530.

Webb, P.P., McIntyre, R.J., Conradi, J., 1974. Properties of avalanche photodiodes. RCA Rev. 35, 234–278.